Development/Plasticity/Repair

PTEN Regulates Dendritic Arborization by Decreasing Microtubule Polymerization Rate

Stephanie A. Getz,[1] Kamran Tariq,[1] Dylan H. Marchand,[2] Conor R. Dickson,[2] James R. Howe VI,[1] Patrick D. Skelton,[1] Wei Wang,[1] Meijie Li,[1] Jeremy M. Barry,[2] Jennifer Hong,[3] and Bryan W. Luikart[1]

[1]Department of Molecular and Systems Biology, Geisel School of Medicine at Dartmouth College, Hanover, New Hampshire 03755, [2]Department of Neurological Sciences, Larner College of Medicine, University of Vermont, Burlington, Vermont 05405, and [3]Department of Surgery and Department of Molecular and Systems Biology, Geisel School of Medicine at Dartmouth College, Hanover, New Hampshire 03755

Phosphatase and tensin homolog (PTEN) is a major negative regulator of the phosphatidylinositol-3-kinase (PI3K)/Akt/mechanistic target of rapamycin (mTOR) pathway. Loss-of-function mutations in *PTEN* have been found in a subset of patients with macrocephaly and autism spectrum disorder (ASD). PTEN loss in neurons leads to somal hypertrophy, aberrant migration, dendritic overgrowth, increased spine density, and hyperactivity of neuronal circuits. These neuronal overgrowth phenotypes are present on *Pten* knock-out (KO) and reconstitution with autism-associated point mutations. The mechanism underlying dendritic overgrowth in *Pten* deficient neurons is unclear. In this study, we examined how *Pten* loss impacts microtubule (MT) dynamics in both sexes using retroviral infection and transfection strategies to manipulate PTEN expression and tag the plus-end MT binding protein, end-binding protein 3 (EB3). We found *Pten* KO neurons sprout more new processes over time compared with wild-type (WT) neurons. We also found an increase in MT polymerization rate in *Pten* KO dendritic growth cones. Reducing MT polymerization rate to the WT level was sufficient to reduce dendritic overgrowth in *Pten* KO neurons *in vitro* and *in vivo*. Finally, we found that rescue of dendritic overgrowth via inhibition of MT polymerization was sufficient to improve the performance of *Pten* KO mice in a spatial memory task. Taken together, our data suggests that one factor underlying PTEN loss dependent dendritic overgrowth is increased MT polymerization. This opens the possibility for an intersectional approach targeting MT polymerization and mTOR with low doses of inhibitors to achieve therapeutic gains with minimal side effects in pathologies associated with loss of neuronal PTEN function.

Key words: autism; cytoskeleton; dendrite; microtubule; navigation; PTEN

Significance Statement

Loss of *Pten* function because of genetic deletion or expression of mutations associated with autism spectrum disorder (ASD), results in overgrowth of neurons including increased total dendritic length and branching. We have discovered that this overgrowth is accompanied by increased rate of microtubule (MT) polymerization. The increased polymerization rate is insensitive to acute inhibition of mechanistic target of rapamycin (mTOR)C1 or protein synthesis. Direct pharmacological inhibition of MT polymerization can slow the polymerization rate in *Pten* knock-out (KO) neurons to rates seen in wild-type (WT) neurons. Correction of the MT polymerization rate rescues increased total dendritic arborization and spatial memory. Our studies suggest that phosphatase and tensin homolog (PTEN) inhibits dendritic growth through parallel regulation of protein synthesis and cytoskeletal polymerization.

Received Sep. 9, 2021; revised Jan. 20, 2022; accepted Jan. 23, 2022.

Author contributions: S.A.G., J.M.B., J.H., and B.W.L. designed research; S.A.G., K.T., D.H.M., C.R.D., J.R.H., P.D.S., W.W., M.L., J.M.B., J.H., and B.W.L. performed research; S.A.G. and P.D.S. contributed unpublished reagents/analytic tools; S.A.G., K.T., J.H., and J.M.B. analyzed data; S.A.G., K.T., J.H., and B.W.L. edited the paper; S.A.G., K.T., and J.M.B. wrote the paper.

This work was supported by National Institutes of Health Grant R01 MH097949 (to B.W.L.) and the Autism Speaks Pilot Grant 7359 (to B.W.L.), the Optical Cellular Imaging Shared Resource and the Norris Cotton Cancer Center at the Geisel School of Medicine at Dartmouth, P30 CA023108, and the National Institutes of Health Grant R01 NS108765 (to J.M.B.).

The authors declare no competing financial interests.

Correspondence should be addressed to Bryan W. Luikart at bryan.w.luikart@dartmouth.edu.

https://doi.org/10.1523/JNEUROSCI.1835-21.2022

Introduction

Phosphatase and tensin homolog (PTEN) is a major negative regulator of the phosphatidylinositol-3-kinase (PI3K)/Akt/mechanistic target of rapamycin (mTOR) pathway (Endersby and Baker, 2008; Chalhoub and Baker, 2009). It dephosphorylates phosphatidylinositol (3,4,5)-triphosphate (PIP3) to phosphatidylinositol (4,5)-biphosphate (PIP2), thereby directly antagonizing the activity of PI3K. Mutations in *PTEN* have been found in a subset of humans with macrocephaly and autism spectrum disorder (ASD; Eng, 2003; Butler et al., 2005; Buxbaum et al., 2007; Hansen-Kiss et al., 2017). *Pten* mouse models

revealed macrocephaly and recapitulation of autism-like behavioral phenotypes (Kwon et al., 2006; Clipperton-Allen and Page, 2014; Tilot et al., 2014; Cupolillo et al., 2016). Loss of *Pten* in neurons leads to somal hypertrophy, aberrant migration, increased spine density, and dendritic overgrowth, resulting in hyperexcitability of neuronal circuits (Kwon et al., 2006; Luikart et al., 2011a; Williams et al., 2015; Getz et al., 2016; Skelton et al., 2020).

Dendritogenesis occurs via regulation of translation and precise mobilization of cytoskeletal networks in response to cell intrinsic and extrinsic cues. mTOR-hyperactivating mutations in neurons have been linked to dendritic overgrowth and aberrant protein translation (Jaworski et al., 2005; Kumar et al., 2005; Lin et al., 2016). Genetic mutations and pharmacologic inhibitors to decrease aberrant protein translation have been successful in reducing dendritic overgrowth in neurons. Further, mutations to reduce +TIP microtubule (MT)-associated proteins and f-actin bundling proteins lead to decreased dendritic complexity. However, the interaction between *Pten* loss, cytoskeletal regulation, and spatial cognition are not well understood.

Here, we examined how *Pten* loss impacts MT dynamics using retroviral infection and transfection strategies to manipulate *Pten* expression and tag the plus-end MT binding protein, end-binding protein 3 (EB3), both *in vivo* and in primary cultured hippocampal neurons. We found that ASD-associated *PTEN* mutations do not regulate dendritic overgrowth, and that *Pten* loss results in neurons sprouting more new dendritic processes compared with wild-type (WT) via live multi-photon microscopy. Further, we found that *Pten* knock-out (KO) dendrites have an increased MT polymerization rate in primary cultured neurons via confocal microscopy. This process was both rapamycin and translation independent. Pharmacological reduction of MT polymerization rate to the level of WT with vinblastine was sufficient to reduce dendritic overgrowth in *Pten* KO neurons *in vitro*. Intrathecal administration of vinblastine *in vivo* rescued dendritic arborization and performance of *Pten* KO mice in a spatial memory task. Taken together, our data suggests that PTEN regulation of cytoskeletal polymerization is necessary to regulate dendrite growth and branching. In the context of other studies demonstrating the necessity for protein translation in this process we suggest that parallel pathways regulating protein translation and cytoskeletal polymerization could provide an intersectional approach to treat features of PTEN-mediated disorders.

Materials and Methods

Experimental design and statistical analysis

Quantitative values reported in the manuscript text are mean ± SEM (n = neurons). Unless otherwise indicated, all statistical comparisons are performed in Stata 15 using the mixed-effect model described in Moen et al. (2016). Pairwise comparisons are made between every condition using the pwcompare algorithm in Stata. All graphs were generated using GraphPad Prism 9 and two-way ANOVA, Kolmogorov–Smirnov and t test were all performed using Prism 9.

Replication-deficient retroviruses

Replication deficient retroviruses used the pRubi construct described previously (Luikart et al., 2011a). pRubi-mCherry-T2A-Cre retrovirus used was described previously (Williams et al., 2015). pRubi-GFP-T2A-Cre was generated by PCR cloning Cre and adding 5'*BsrG1* and 3'EcoRI sites, then ligating the product into pGemT-easy. Cre was cut with *BsrG1,* annealed to the T2A oligo, ligated into pGemT-easy, then cut with *BsrG1* and ligated into the lentiviral vector FUGW. This FUG-T2A-Cre was digested with SacII and put into the pRubi backbone to create the retroviral version.

To generate pRubi-X(XbaI)-T2A-Cre, GFP was then removed through a sequential digestion with EcoRI and XbaI, yielding pRubi-"XbaI"-T2A-Cre. *PTEN*, *H93R*, and *D252G* were cloned into the XbaI site using the following primers (sense 5′-TCTAGAACCATGACAGCCATACATCAAAGAGATCG-3′; antisense 5′-TCTAGAGACTTTTGTAATTTGTGTATGCTGATCTTC-3′).

To the generate EB3-GFP retrovirus, EMTB-3xGFP plasmid (EB3-GFP; a gift from William Bement; Addgene plasmid #26741; http://n2t.net/addgene:26741; RRID:Addgene_26741; Miller and Bement, 2009) was cut with AvaI/AgeI, and cloned into the *AgeI* site of pRubi to generate pRubi-EB3-GFP. Retroviral packaging was performed as described previously (Fricano-Kugler et al., 2016).

Animals

All procedures were approved by both the Dartmouth Institutional Animal Care and Use Committee, and the Association for Assessment and Accreditation of Laboratory Animal Care Review Board. Mice of either sex were used. *Pten* $^{flox/flox}$ (B6.129S4-*Pten*^{tm1Hwu}/J) mice were backcrossed into the C57BL/6J background at least five generations. *Pten* $^{Flox/Flox}$x tdTomato (Ai14) $^{Flox/Flox}$ mice were generated by crossing *Pten* $^{Flox/Flox}$ (B6.129S4-*Pten*^{tm1Hwu}/J) mice to tdTomato (Ai14) $^{Flox/Flox}$ (B6;129S6-*Gt(ROSA)26Sor*$^{tm14(CAG-TdTomato)Hze}$/J).

Stereotaxic injection

Stereotaxic injection was performed as described previously (Williams et al., 2015, 2016; Getz et al., 2016). Briefly, postnatal day (P)7 mice were anesthetized with isoflurane, injected with 2 µL of virus at a rate of 0.3 µl/min at y + 1.55 mm and x ± 1.30 mm relative to λ and the z-coordinates were −2.3, −2.2, −2.1, −2.0 mm, with 25% of the total volume of virus injected at each depth. Upon completion of injection we waited 1 min before slowly bringing the needle out of the skull.

Fixed-tissue immunohistochemistry, imaging, and analysis

Immunohistochemistry was performed as described previously (Luikart et al., 2011b; Fricano et al., 2014). Primary antibodies were chicken anti-GFP (1:3000; Abcam) and rabbit anti-mCherry (1:3000; Abcam). Secondary antibodies include Alexa Fluor 488 anti-chicken (GFP), and Cy3 anti-mouse (mCherry; 1:200; Jackson ImmunoResearch).

Z-stacks for soma size analysis were taken on a either a Zeiss LSM510 with either a 20×/0.75 μm plan-apochromat lens with 2× zoom, at 512 × 512, and a 2-μm z-step, or a CCD camera (Hamamatsu) fitted on a spinning disk confocal microscope (BX61WI; Olympus) controlled by IPLab 4.0 software (BD Biosciences) with a 40×/1.3 µm oil emersion lens. Soma size was analyzed in the same manner as described previously (Fricano et al., 2014) by circling somas at their maximum circumference in ImageJ/Fiji (NIH). We noted no difference in analysis of morphologic values using these different imaging modalities.

Migration was quantified as the distance of a cell from the granule cell layer (GCL)/hilus border divided by the local thickness of the GCL (Perederiy et al., 2013; Getz et al., 2016). Total dendritic arborization was analyzed by first collecting 150-µm sections from the hippocampus. z-Stacked images were taken on Zeiss LSM510 laser-scanning confocal at 20×/0.75 plan-apochromat lens with 1× zoom, at 512 × 512, 4× averaging, and a 2-μm z-step. We analyzed neurons with cell bodies in the center 50 µm of the 150-µm image stacks to ensure that there was no significant arborization outside of the 150-µm-thick section. Neurons were reconstructed using Neurolucida, and analyzed with Neurolucida Explorer (Williams et al., 2015). For reconstructions after *in vivo* vinblastine/vehicle injections the updated Neurolucida 360 software package was employed with higher resolution 1024 × 1024 image stacks (all other parameters the same).

Acute slice generation

Acute live slice generation was previously described previously (Williams et al., 2015; Skelton et al., 2019). Briefly, mice were anesthetized with tribromoethanol and perfused with an ice cold cutting solution containing the following: 110 mM choline-Cl, 10 mM D-glucose, 7 mM $MgCl_2$, 2.5 mM KCl, 1.25 mM NaH_2PO_4-$2H_2O$, 0.5 mM $CaCl_2$, 1.3 mM NA-ascorbate, and 25 mM $NaHCO_3$, bubbled with 95% O_2-5%

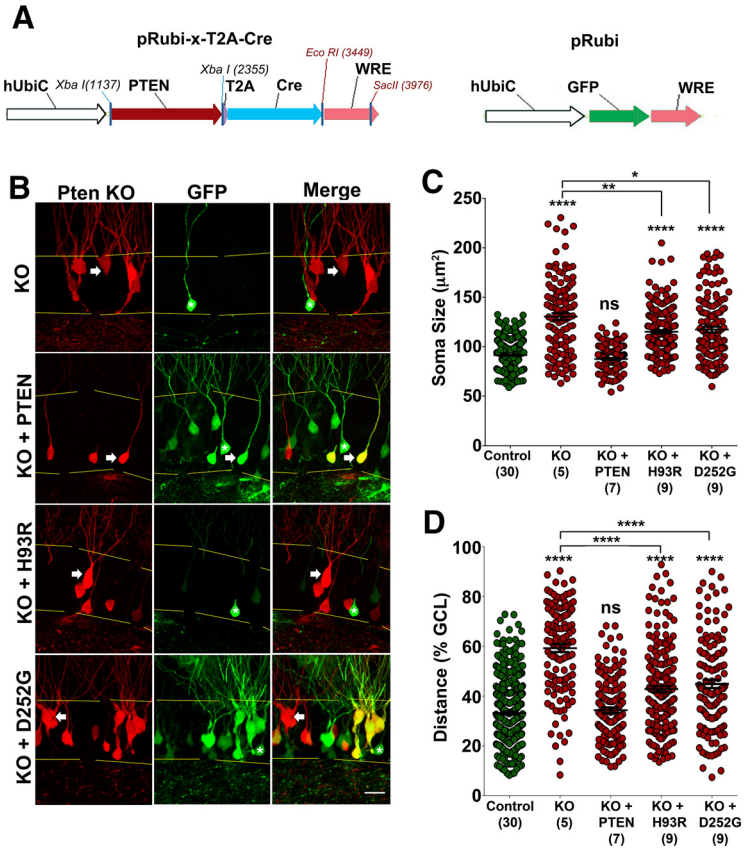

Figure 1. ASD-associated PTEN point mutations do not rescue neuronal hypertrophy or migration. Schematic of retroviruses expressing Cre recombinase and human PTEN variants (pRubi-x-T2A-Cre) that were co-injected with a control retrovirus expressing only GFP (pRubi; ***A***). *In vivo* injection of virus into the dentate gyrus of *Pten*$^{Flox/Flox}$xtdTomato (Ai14)$^{Flox/Flox}$ mice at P7 and histology was performed at 24 DPI. Expression of Cre only (KO) resulted in neuronal hypertrophy while WT PTEN (KO+PTEN) rescued the hypertrophy. Neither H93R (KO+H93R) nor D252G (KO+D252G) rescued hypertrophy (***B***, quantified in ***C***). *Pten* KO neurons migrate farther into the GCL compared with controls, while reconstitution with WT PTEN rescues this effect. PTEN H93R or D252G expression do not rescue, displaying migration farther into the GCL compared with controls (***B***, quantified in ***D***). Arrows in ***A*** illustrate *Pten* KO or KO+ASD mutation, while asterisks illustrate control neurons. Scale bars: 50 μm (***B***). The numbers in parenthesis represent animal number. Statistical comparisons are against control or indicated by brackets; *$p < 0.05$, **$p < 0.01$, ***$p < 0.001$, ****$p < 0.0001$.

CO_2; 290-μm-thick sections were generated through the hippocampus on a VT1200s vibratome (Leica), Slices were stored in artificial CSF (aCSF) at room temperature. The contents of aCSF are as follows: 125 mM NaCl, 25 mM $NaHCO_3$, 2.5 mM KCl, 1.25 mM NaH_2PO_4, 2.0 mM $CaCl_2$, 1.0 mM $MgCl_2$, and 25 mM D-glucose, bubbled with 95% O_2-5% CO_2.

Live-tissue multiphoton imaging and analysis

Multiphoton microscopy (Ultima In Vivo, Prairie Technologies/Bruker) was used to capture a *z*-series (0.5-μm step) through the entire dendritic arbor of retrovirus-infected granule neurons every 2 min for 1 h from acute slices collected between 7 and 12 d postinjection (DPI). Neurons were imaged with 60 × 1.0 NA lens, with 4× averaging, 2.5× zoom, at either 512 × 512 pixels or 1024 × 1024 pixels, and a 1.2-μs dwell time. Slices were perfused with aCSF bubbled with 95% O_2, 5% CO_2 at 37°C. Fluorescence was stimulated by either 860 nM or 920 nM using a Chameleon tunable laser (Coherent).

Images were analyzed in ImageJ/Fiji. Images were first converted from a stack to a hyperstack, and channels were separated into green (MT) and red (cytoplasm). We found bleed-through from the red (cytoplasm) channel into the green (MT) channel by ~15%. To correct for that, the red channel was multiplied by 0.15 and then the green channel was subtracted by the red channel. The n-Tracer1.1.1 alignmaster plugin (Roossien et al., 2019) was used to correct for photobleaching over time. Finally, channels were merged, and the rigid body StackReg plugin (Thévenaz et al., 1998) was used to control for *x*-drift and *y*-drift.

To analyze these images the entire length of a primary dendritic arbor was traced to measure the length over which new processes could emerge. To analyze new processes, a region of interest (ROI) was selected surrounding the process using the polygon selection tool. Processes were then tracked over time. Number of new processes/μm/h was obtained by counting the number of new processes emerging per micrometer per hour and averaged for each neuron. MT (ΔMT_{Int}) and cytoplasmic ($\Delta Cyto_{Int}$) intensity changes were obtained by separating MT (green) and cytoplasmic (red) channels, thresholding each process within the ROI and following those processes over time. MT intensity change was calculated as follows: $\Delta MT_{Int} = (t_2MT_{Int} - t_1MT_{Int})/t_1Cyto_{Int}$. Cytoplasmic intensity change was calculated as follows: $\Delta Cyto_{Int} = (t_2Cyto_{Int} - t_1Cyto_{Int})/t_1Cyto_{Int}$. Values were plotted and fitted with a Gaussian function and population distribution was compared between WT and KO processes. For examination of ΔMT_{Int} and $\Delta Cyto_{Int}$ as a per-cell average the absolute value of the intensity change was used so that decreasing intensity (negative values) and increasing intensity (positive values) do not cancel when averaged. Only cells with at least one new process persisting for at least five time frames were averaged.

Primary culture imaging and immunocytochemistry

Primary neurons were cultured and transfected as described previously (Luikart et al., 2008). Live imaging of dendritic growth cones from primary hippocampal cultures were collected on a Zeiss LSM-800 with Airyscan with a 63×_1.4 NA_190WD lens with 2× zoom, 4× averaging, at 1024 × 1024 pixels, a *z*-series of two slices with definite focus, and a time interval of about 5 s (frame rate of ~2.09 s) for 10 min, or on a Zeiss LSM-880 with Airyscan 63-×_1.4 NA_190WD lens with 2× zoom, 4× averaging, at 1024 × 1024 pixels, a *z*-series of two slices, and a time interval of 4.16 s (frame rate of 2.08 s) for ~10 min. All primary cultured neurons were incubated at 37°C with 5% CO_2 during imaging. For drug experiments, drugs were added to primary cultures immediately before imaging and each culture was imaged for up to 4 h. To analyze MT polymerization rate, channels were separated and *z*-projected. The lookup table on the growth cone was changed to grayscale and inverted, such that EB3-puncta were black. Puncta were tracked with the MTrackJ plugin on ImageJ/Fiji (NIH; Meijering et al., 2012). We noted no difference in EB3 puncta quantification as imaged on the LSM-800 or 880.

After imaging, primary cultures were fixed by first adding equal volume warmed 4% sucrose and 4% paraformaldehyde (PFA) in PBS to cultures, such that 2% of the total volume is PFA for 5–10 min. Following that, the solution was replaced with 4% sucrose and 4% PFA in PBS for 5–10 min. Cultures were then stained as described previously (Luikart et al., 2008).

Imaging fixed primary cultures

For immunocytochemistry, cells were imaged on a Zeiss LSM-800 with Airyscan with a 20×/0.8 plan-apochromat lens with 1.5× zoom, at 512 × 512, with 4× averaging, and a 2-μm *z*-step. For chronic vinblastine treatment, cells were imaged on a Zeiss LSM-800 with Airyscan with a 20×/0.8 plan-apochromat lens with 0.6× zoom, 1× averaging, at 2048 × 2048, and a 1-μm *z*-step. Neurons were reconstructed as described above.

Table 1. Granule neuron soma size and position values

	Raw soma size (μm^2)	Raw neuron position (% of GCL)	Neurons	Animals	Corrected soma size (μm^2)	Corrected neuron position (% of GCL)	Neurons	Animals
Control	91.4 ± 0.6	33.2 ± 0.6	471	30	91.4 ± 0.6	33.2 ± 0.6	471	30
Pten KO	130.5 ± 3.4	59.3 ± 1.6	127	5	151.3 ± 3.0	60.5 ± 1.6	86	5
KO + PTEN	87.5 ± 1.1	34.4 ± 1.1	137	7	87.5 ± 1.1	34.4 ± 1.1	137	7
KO + H93R	115.0 ± 1.7	42.8 ± 1.2	195	9	129.4 ± 1.7	47.0 ± 1.5	118	9
KO + D252G	117.3 ± 2.9	44.9 ± 1.6	133	9	143.0 ± 3.1	52.3 ± 2.1	68	9

The average soma cross sectional area (size) and position in the GCL as a % of the total width of the GCL for WT control neurons, *Pten* KO neurons, and KO neurons with reconstitution of human WT, H93R, or D252G PTEN. Raw values include every tdTomato-positive cell. Corrected values exclude tdTomato-positive cells with soma size <106.8 μm^2. All values are reported as mean ± SEM.

Spatial accuracy behavior

The goal of spatial accuracy training was to shape food restricted mice (85% of baseline body weight) to associate a visible bottle cap cue, placed roughly in the middle of one of the arena quadrants, with automated food reward. As training progressed, the shaping procedure reduced the size of the reward zone and the amount of time required to trigger a pellet release from an overhead feeder would increase. The goal cue would then be removed to test the animal's ability to flexibly associate the object with both the original training location and novel spatial locations during probe trials (Bures et al., 1997; Kubie et al., 2007; Mouchati et al., 2020).

Over the course of training, the goal zone diameter ranged down to 10% of the 76-cm diameter arena. The task has two modes for spatial behavior. One mode is for goal-directed navigation when the animal is seeking the goal zone and the other for foraging for a food reward after the pellet has been dropped into a random arena location following a successful pause within the goal zone. The visible and hidden versions of the spatial accuracy task were modeled after the cue and place navigation tasks in the Morris water maze (Morris et al., 1982). Hippocampal lesions cause a significant and long-lasting place navigational impairment that cannot be attributed to motor, motivational or reinforcement deficits. In contrast to the water maze task, the spatial accuracy task allows for continuous measurement of multiple goal navigation epochs and spatial memory measurements in one session (Mouchati et al., 2020).

Mouse location was tracked and recorded via a firewire camera (30 Hz sampling rate) placed over the arena and analyzed with Biosignal software (Tracker, Bio-signal Group Corp) and custom software (MATLAB v R2019A, MathWorks). Training began with a 2-cm diameter white bottle cap used as a visible goal. The bottle cap was placed ¾ from the arena wall to the arena center in the northeast quadrant. A polarizing cue card (color code gray 9.5; Color-Aid Corp.) was placed along the north sector of the arena wall, covering ~450 of arc. Animals were advanced to successive visible goal phases after reaching a criterion of 20 rewards. In phases 1–4 of training, 500-ms dwell-time in a target zone successively ranging in diameter from 51 cm (phase 1), 28 cm (phase 2), 19 cm (phase 3), and 15 cm (phase 4) elicited a +5V TTL pulse via a peripheral component interconnect. This pulse triggered release of a food pellet reward (Bioserv; 20-mg dustless precision pellets) from a custom overhead feeder, which fell to a random arena location. A refractory reward period of 5 s was set to encourage the animal to leave the target area and forage for the fallen pellet before returning to the goal zone to trigger another pellet. In this manner, measures of continuous navigation to and from the goal zone were possible over the course of each 30-min training session. In phases 5–7, the threshold for target dwell-time was raised to 750 ms, 1 s, and 1.2 s

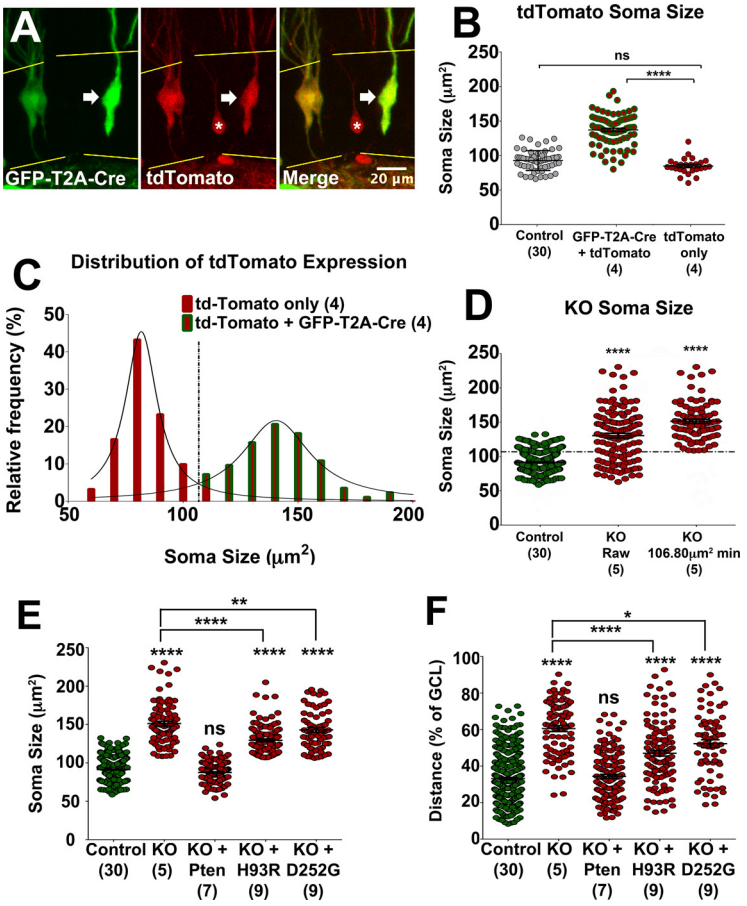

Figure 2. Expression of tdTomato in tdTomato (Ai14) mice. GFP-T2A-Cre-expressing retrovirus was injected into the dentate gyrus of *Pten* $^{Flox/Flox}$ x tdTomato (Ai14) $^{Flox/Flox}$ mice at P7. In doing so, Cre-positive *Pten* KO neurons are both GFP-T2A-Cre-positive and tdTomato-positive, while tdTomato-positive neurons without GFP expression are WT neurons displaying tdTomato expression independently of GFP-T2A-Cre expression. The yellow lines indicate the boundaries of the GCL. The asterisks indicate a cell with tdTomato expression but lacking GFP expression, while the arrow indicates a GFP-T2A-Cre-positive and tdTomato-positive *Pten* KO neuron (***A***). Soma size analysis of co-labeled GFP-T2A-Cre and tdTomato positive neurons compared with control (GFP-only expressing neurons from an independent set of animals) reveals GFP-T2A-Cre positive neurons were larger than tdTomato positive neurons, while tdTomato only neurons were the same size as WT control neurons (***B***). Soma size was then expressed as a frequency distribution with one peak for both GFP-T2A-Cre-positive and tdTomato-positive at around 140–150 μm^2, indicative of *Pten* KO neurons. Another peak was only tdTomato-positive and had a peak soma size at around 80 μm^2, indicative of WT neurons. The distribution was fit using the nonlinear Lorentzian function (tdTomato $R^2 = 0.99$, GFP-T2A-Cre $R^2 = 0.95$) to find that these two peaks crossed at 106.80 μm^2 (***C***). A cutoff of 106.80 μm^2 was then applied to the raw soma size values to eliminate cells ectopically expressing tdTomato from our morphologic analyses of *Pten* KO neurons (***D***). This 106.80-μm^2 cutoff was applied to the raw data for soma size and neuronal position (from Fig. 1) to generate transformed values for soma size (***E***) and position (***F***) that are more accurate absolute values for these measures. The numbers in parenthesis represent animal number. Statistical comparisons are against control or indicated by brackets; $^*p < 0.05$, $^{**}p < 0.01$, $^{***}p < 0.001$, $^{****}p < 0.0001$.

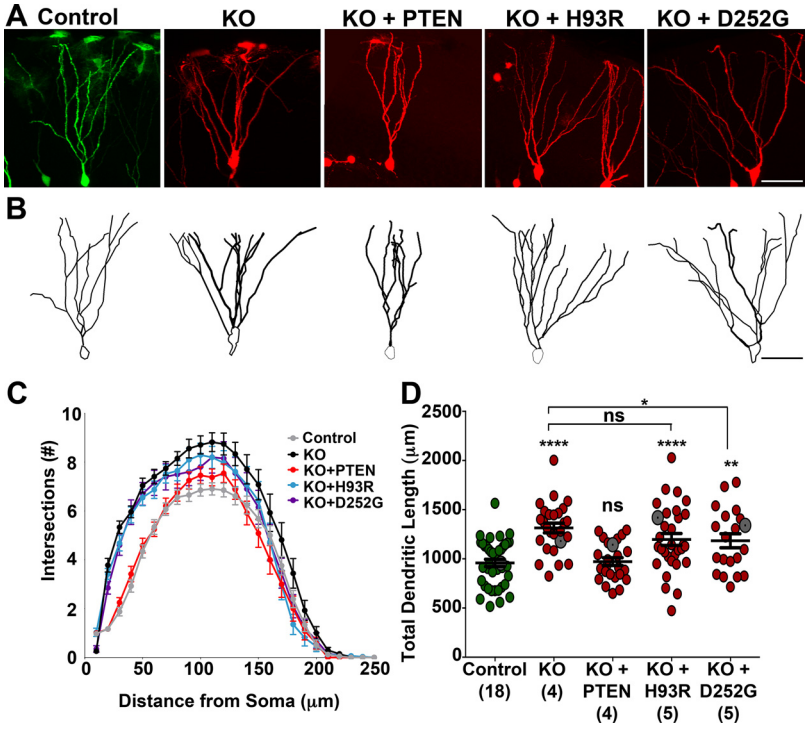

Figure 3. Autism-associated PTEN mutations fail to rescue increased dendritic arborization. P7 $Pten^{Flox/Flox}$x tdTomato $(Ai14)^{Flox/Flox}$ mice were co-injected with a GFP-only control retrovirus and a Cre retrovirus to KO *Pten* and express PTEN, H93R, or D252G. Neurons were imaged and traced at 24 DPI (***A***). Neurolucida reconstructions of representative neurons (***B***). All reconstructions can be seen in Figure 4. Sholl analysis of intersections reveals *Pten* KO neurons have more branching than control, and reconstitution with PTEN was similar to control. Reconstitution with H93R or D252G also resulted in more branching than control (***C***). KO neurons had increased total dendritic length compared with control, while reconstitution with PTEN was similar to control and H93R or D252G displayed increased total dendritic length compared with controls (***D***). Gray dots denote the total dendritic length of the representative images and traces in ***A***, ***B*** (***D***). Scale bars: 50 μm (***A***, ***B***). The numbers in parenthesis represent animal number. Statistical comparisons are between the GFP-only control unless indicated by brackets; $*p < 0.05$, $**p < 0.01$, $***p < 0.001$, $****p < 0.0001$ using a mixed-effect model and pwcompare.

consecutively. Finally, in phase 8 of training the visible goal cue was removed. To prevent the use of olfactory cues in these sessions, the floor was rotated 45° and cleaned with soap and water and then 70% ethanol. In these hidden goal training sessions, the animal's spatial behavior provided a proxy measure of self-localization relative to the estimated goal zone location as determined by stationary room and arena cues. Previous studies with goal zones at similar distances from polarizing cue cards found that behavioral choices correlated with place field location (Lenck-Santini et al., 2001). After reaching the 20-goal criterion in the original goal location, pairs of probe test sessions were conducted in each of the three remaining quadrants; one with the visible goal cue and then another without the goal cue. These probes were typically separated by ~10 min while the experimenter cleaned and rotated the floor. The mouse only triggered food reward in the newly rotated goal location. Visible/hidden goal tests were conducted in each quadrant at the same distance from the arena wall as the original training location. Only one pair of visible/hidden goal probe trials were conducted per day.

Results

Neurons expressing ASD-associated PTEN mutations have increased dendritic arborization

To determine whether expression of ASD-associated *PTEN* point mutations support normal dendritic development, we created a retrovirus to express human PTEN or the ASD-associated H93R or D252G mutations and Cre-recombinase (Fig. 1*A*). To KO endogenous *Pten* and fluorescently label neurons, we injected these retroviruses into the dentate gyrus of $Pten^{Flox/Flox}$ x tdTomato$(Ai14)^{Flox/Flox}$ mice on P7 (Fig. 1*A*,*B*). We co-injected the Cre retrovirus with a control retrovirus that expressed GFP-only so that WT and *Pten* manipulated cells could be compared within the same animal. The retroviral system results in discrete labeling of newborn neurons, allowing us to perform detailed reconstructions of neurons in a homogenous developmental state (24 DPI). Quantitative analysis of soma size and migration distance indicated that loss of *Pten* resulted in hypertrophy and increased migration. The reconstitution of WT human PTEN was able to rescue these effects. However, the ASD mutations were unable to rescue them (Fig. 1*B–D*; raw values, Table 1).

We noted that some tdTomato positive cells displayed WT soma sizes. We found ectopic tdTomato expression in both uninjected Ai14 mice and, to a greater degree, in Ai14 mice injected with Cre-expressing retrovirus. This resulted in quantitative measures of soma size and migration distance for Cre-expressing neurons that were smaller than in previous studies with techniques that did not rely on the Ai14 allele (Getz et al., 2016). To eliminate cre-independent td-Tomato-expressing cells from our quantitative measures, we injected a retrovirus expressing GFP-T2A-Cre into the $Pten^{Flox/Flox}$ x tdTomato$(Ai14)^{Flox/Flox}$mice and noted tdTomato positive neurons that did not express the GFP-T2A-Cre and had WT soma sizes (Fig. 2*A*,*B*). This indicates that in a subset of neurons, recombination at the Ai14 allele can occur independently of Cre virus genomic integration and recombination of the $Pten^{Flox/Flox}$ allele. To avoid including WT neurons displaying ectopic tdTomato expression, we analyzed the distribution of soma sizes for neurons expressing tdTomato only and those expressing tdTomato and GFP-T2A-Cre (Fig. 2*C*). We found a cutoff of cells with soma areas below 106.8 μm^2 allowed us to conservatively exclude cells with Cre-independent td-Tomato expression (Fig. 2*D*). We, then applied this cutoff for the quantitative measurements of GFP-T2A-Cre positive neurons in $Pten^{Flox/Flox}$ x tdTomato$(Ai14)^{Flox/Flox}$ (Fig. 2*E*,*F*; corrected values, Table 1). This yielded quantitative measures for soma size and migration with absolute values for WT and *Pten* KO neurons are the same as from previous studies using retroviruses to KO *Pten in vivo* (Getz et al., 2016). Further, the absolute values for soma size of neurons expressing ASD-associated PTEN mutations was also equivalent to the previously published lentiviral *Pten* KO data (Fricano-Kugler et al., 2018).

We next measured dendritic arborization of *Pten* KO neurons after reconstitution of PTEN, H93R, or D252G (Figs. 3, 4; Table 2). Sholl analysis revealed that *Pten* KO neurons had an increased number of intersections compared with control, while human PTEN reconstitution resulted in neurons indistinguishable from control (Fig. 3*C*). Reconstitution with H93R or D252G

resulted in an increase in intersections compared with control neurons (Fig. 3*C*). The initial increase in intersections from 1 to 50 µm is because of multiple primary dendrites emerging from the soma of KO, H93R, and D252G conditions (Fig. 3*A–C*). Total dendritic length was increased in *Pten* KO neurons, and reconstitution with human PTEN reduced the length to control levels (Fig. 3*D*). Reconstitution with H93R or D252G was unable to restore total dendritic length to control levels (Fig. 3*D*). Thus, ASD-associated PTEN point mutations are incapable of regulating normal dendritic arborization.

Pten loss leads to increased sprouting of new dendritic processes

To examine the dynamics of dendritic overgrowth we performed live two-photon imaging experiments of dendritic growth and MT dynamics in acute hippocampal slices. To label growing neurons, we co-injected mCherry-T2A-Cre-expressing retroviruses with retroviruses tagging the plus-end MT EB3 with GFP (pRubi-GFP; pRubi-EB3-GFP) into the hippocampal dentate gyrus of either $Pten^{Flox/Flox}$x tdTomato(Ai14)$^{Flox/Flox}$ mice or tdTomato (Ai14)$^{Flox/Flox}$ mice on P7. Thus, one group of animals harbored retrovirally-infected *Pten* KO neurons ($Pten^{Flox/Flox}$x tdTomato(Ai14)$^{Flox/Flox}$) expressing both tdTomato and EB3-GFP; the other group harbored retrovirally-infected WT neurons ($Pten^{wt//wt}$ tdTomato (Ai14)$^{Flox/Flox}$) expressing tdTomato and EB3-GFP. We generated acute slices between 7 and 12 DPI because dendrites are undergoing rapid growth in this window (Williams et al., 2015).

To image dendrite growth, we collected *z*-series through the entirety of the dendritic arbor every 2 min for 1 h. We first analyzed new process emergence and stability. We found that more new processes sprouted from *Pten* KO neurons over time than did in WT neurons [*Pten* KO = 0.058 ± 0.0098 processes/µm/h (n = 30); WT = 0.027 ± 0.0048 processes/µm/h (38); p = 0.005, unpaired t test with Welch's correction; Fig. 5*A*, *B*]. Process stability was examined by counting the number of processes emerging within the first 30 min of imaging and tracking the presence of each of those processes for up to 30 min. We found no significant difference in the stability of new dendritic processes between *Pten* KO and WT neurons [*Pten* KO = 11.87 ± 1.21 min (30); WT = 16.46 ± 2.00 min (38); $p > 0.05$, unpaired t test with Welch's correction]. These data suggest *Pten* KO neurons sprout more new processes, which stabilize at similar rates to WT controls.

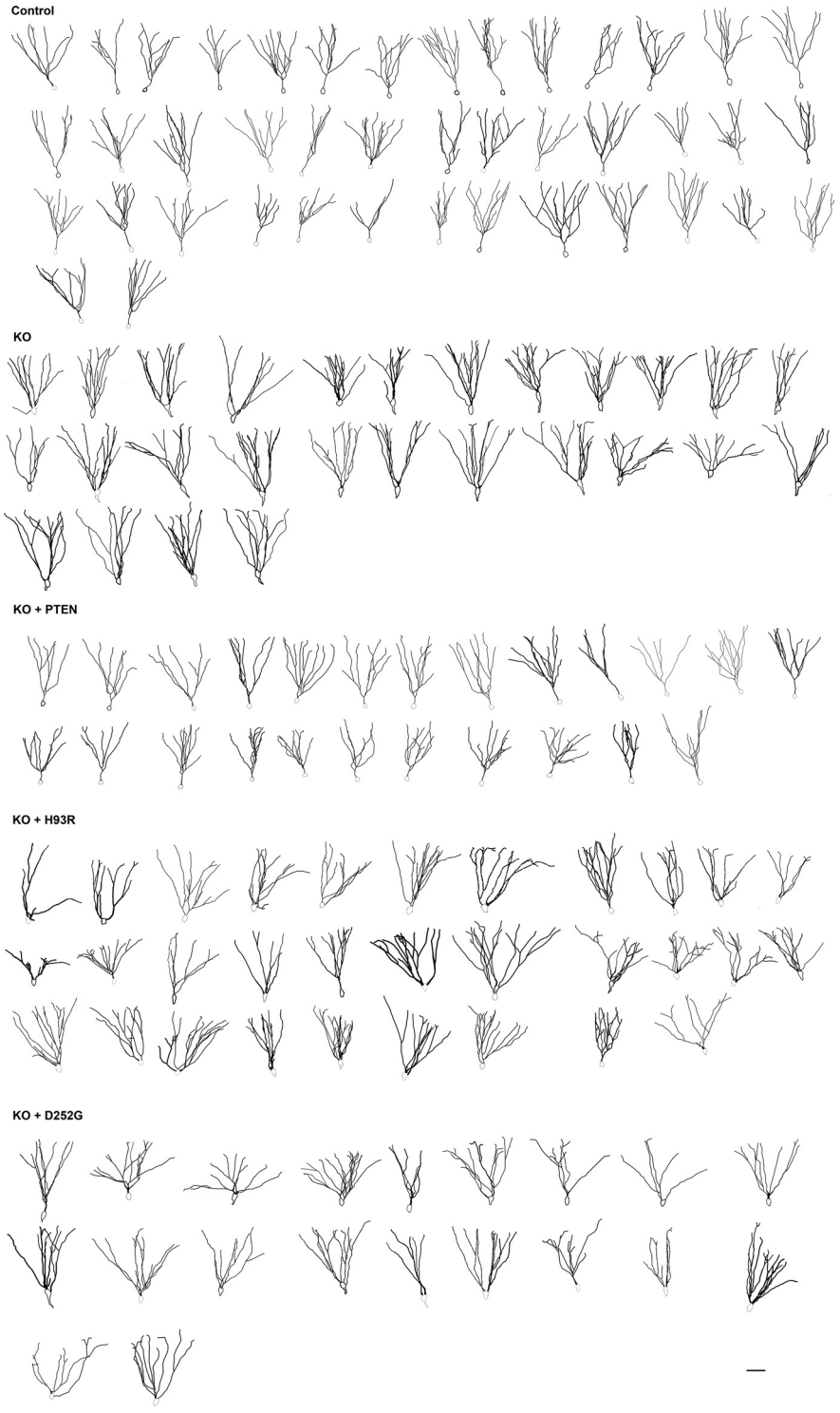

Figure 4. Neurolucida dendritic reconstructions. Line drawings of neuronal reconstructions for fluorophore-only expressing neurons (control), $Pten^{flx/flx}$; Cre+ (KO), *Pten* KO neurons with human *PTEN* reconstitution (KO + PTEN), *Pten* KO with *PTEN* H93R reconstitution (KO + H93R), and *Pten* KO with *PTEN* D252G reconstitution (KO + D252G). Scale bar: 50 µm.

Pten loss increases MT dynamics

To determine whether there was a change in MT dynamics related to loss of *Pten*, we examined the change in EB3-GFP and tdTomato intensity within new processes over time (Fig. 6). Because of the large image stacks required to capture the growth

Table 2. Granule neuron total dendritic arborization value

	Average total dendritic length (μm)	Neurons	Animals
Control	958 ± 36.7	41	18
Pten KO	1314 ± 48.8	27	4
KO + PTEN	971 ± 39.9	24	4
KO + H93R	1191 ± 60.4	31	5
KO + D252G	1185 ± 71.4	20	5

Average total dendritic length for WT control neurons, *Pten* KO neurons, and KO neurons with reconstitution of human WT, H93R, or D252G PTEN. All values are reported as mean ± SEM.

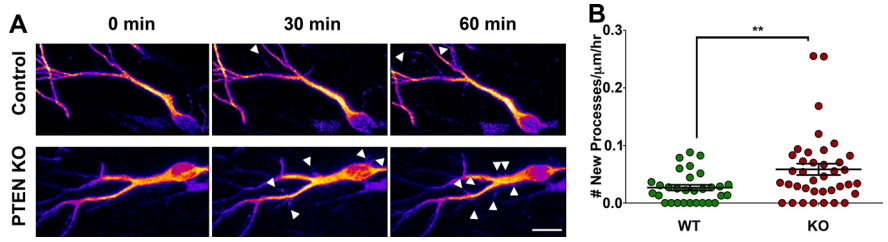

Figure 5. *Pten* loss increases sprouting of new processes. Retroviruses expressing mCherry-T2A-Cre and EB3-GFP were co-injected into the hippocampal dentate gyrus of either tdTomato(Ai14) $^{Flox/Flox}$ (Control) or *Pten* $^{Flox/Flox}$ x tdTomato(Ai14) $^{Flox/Flox}$ (*Pten* KO) mice at P7. In doing so, control (top) and *Pten* KO (bottom) neurons endogenously express tdTomato allowing two-photon imaging of whole dendritic arbors over time. The intensity of the tdTomato in these images is indicated using the fire lookup table in ImageJ. Acute hippocampus slices were collected at 7–12 DPI and imaged every 2 min for 1 h. New dendritic processes were tracked over time (arrowheads; ***A***) to find that *Pten* KO neurons sprouted more new processes per micrometer of dendrite length per hour as compared with WT (**$p = 0.005$, unpaired *t* test with Welch's correction; WT: 30 neurons from 14 animals; KO: 38 neurons from 15 animals; ***B***). Scale bar: 20 µm.

of the entire dendritic arbor, the time interval (every 2 min) was insufficient to track individual EB3-GFP puncta. Therefore, to assay MT dynamics, the change in MT [$\Delta MT_{Int} = (t_2MT_{Int} - t_1MT_{Int})/t_1Cyto_{Int}$] or cytoplasmic [$\Delta Cyto_{Int} = (t_2Cyto_{Int} - t_1Cyto_{Int})/t_1Cyto_{Int}$] intensity was tracked between frames for the lifetime of individual processes. MT (ΔMT_{Int}) and cytoplasmic ($\Delta Cyto_{Int}$) intensity changes were plotted in a histogram and the distribution was fit with a Gaussian function (ΔMT_{Int} R^2 WT: 0.99, KO: 0.98; $\Delta Cyto_{Int}$ R^2 WT: 0.99, KO: 0.99). There was a broader distribution of MT intensity change within *Pten* KO dendritic processes, as compared with control ($p = 0.005$, Kolmogorov–Smirnov test; WT: 551 processes, KO: 1109 processes; Fig. 6*B*). However, there was no difference in cytoplasmic intensity change of *Pten* KO and control neurons ($p = 0.184$, Kolmogorov–Smirnov test; WT: 551 processes, KO: 1109 processes; Fig. 6*C*). We next compared the average of the absolute values of [$\Delta MT_{Int} = (t_2MT_{Int} - t_1MT_{Int})/t_1Cyto_{Int}$] for WT versus KO neurons and found that there was an increased change in intensity for EB3-GFP compared with tdTomato [*Pten* KO = 0.0447 ± 0.0034 au/min ($n = 27$); WT = 0.0336 ± 0.0057 au/min (20); $p < 0.01$, Mann–Whitney test; Fig. 6*D*]. This change was not significant when comparing cytoplasmic intensity of tdTomato over time [*Pten* KO = 0.0413 ± 0.0031 au/min (27); WT = 0.0342 ± 0.0038 au/min (20); $p > 0.05$, Mann–Whitney test; Fig. 6*E*]. Given the punctate nature of the EB3-GFP signal, we interpret the intensity change as an increase in the likelihood for puncta to appear or disappear within a new dendritic process between two image intervals.

Pten KO dendritic growth cones have an increased MT polymerization rate

To more directly address whether *Pten* loss impacts MT dynamics, we used primary hippocampal cultures from either *Pten*$^{Flox/Flox}$ or *Pten*$^{Flox/Flox}$ x tdTomato(Ai14)$^{Flox/Flox}$ mice at P0/1. Cultures were co-transfected with either mCherry-T2A-Cre-expressing plasmids with EB3-GFP-expressing plasmids (KO plate), or mCherry-expressing plasmids with EB3-GFP-expressing plasmids (WT plate). Dendritic growth cones from transfected primary hippocampal cultures were imaged via confocal microscopy between 5 and 7 d *in vitro* (DIV). We acquired two-image stacks every 4–5 s allowing us to track individual EB3-GFP puncta. EB3-GFP puncta velocities provide a measure of MT polymerization rate (Fig. 7; Stepanova et al., 2003; Ketschek and Gallo, 2010). We found an increased MT polymerization rate within dendritic growth cones from *Pten* KO neurons, as compared with WT [*Pten* KO = 0.12 ± 0.005 µm/s (30); WT = 0.076 ± 0.004 µm/s (27); $p = 0.0001$, unpaired *t* test with Welch's correction; Fig. 7*A*,*B*].

We next examined plus-end MT stability. We quantified the number of EB3 puncta appearing, disappearing, and the total number of puncta present at any given time point within a dendritic growth cone. We normalized those results to growth cone area and obtained an average per neuron. We analyzed the ratios of either the number of puncta appearing/total, disappearing/total, or appearing/disappearing within a given growth cone. We found there was no difference in the number of puncta appearing/total, number of puncta disappearing/total, and number of puncta appearing/disappearing [appearing/total, *Pten* KO = 0.006 ± 0.0005 puncta/s (30); WT = 0.005 ± 0.0006 puncta/s (27), $p = 0.32$; disappearing/total, *Pten* KO = 0.0057 ± 0.005 puncta/s (30); WT = 0.0047 ± 0.0006 puncta/s (27), $p = 0.35$; appear/disappear, *Pten* KO = 1.00 ± 0.016 puncta/s (30); WT = 0.99 ± 0.004 puncta/s (27), $p = 0.75$, unpaired *t* test with Welch's correction]. These results suggest that *Pten* loss in primary hippocampal cultured dendritic growth cones does not significantly impact MT plus-end stability but instead impacts MT polymerization rate.

PTEN regulates MT polymerization rate independently of mTORC1

We treated cultured neurons with pharmacologic inhibitors of mTORC1 and protein synthesis to determine whether the effect on MT polymerization rate was independent of mTORC1 regulation of protein synthesis. Acute inhibition of mTORC1 (rapamycin 25 nM; RAPA) or protein synthesis (cycloheximide 35 μM; CHX) was unable to reduce MT polymerization rate in WT [WT Veh = 0.08 ± 0.004 µm/s (14) vs WT Rapa = 0.08 ± 0.006 µm/s (17); $p = 0.999$; WT Veh = 0.099 ± 0.007 µm/s (8) vs WT CHX = 0.086 ± 0.004 µm/s (16) $p = 0.999$] and *Pten* KO neurons from RAPA-treated or CHX-treated cultures [KO Veh = 0.11 ± 0.004 µm/s (18) vs KO Rapa = 0.11 ± 0.005 µm/s (24) $p = 0.999$; KO Veh = 0.12 ± 0.007 (19) vs KO CHX = 0.13 ± 0.006 (22) $p = 0.248$, two-way ANOVA with Bonferroni's *post hoc*]. In both cases, however, *Pten* KO neurons from RAPA-treated or CHX-treated cultures had an increased MT polymerization rate, as compared with WT neurons from vehicle-treated cultures (WT Veh vs KO Rapa $p = 0.016$; WT Veh vs KO CHX $p = 0.018$, two-way ANOVA with Bonferroni's *post hoc*). For positive controls, we found a qualitative reduction in p-S6(235, 236) staining in

RAPA-treated cultures and inhibition of protein synthesis in a puromycin incorporation assay of CHX-treated cultures (data not shown).

Vinblastine rescues dendritic overgrowth of *pten* KO neurons *in vitro*

We next tested whether inhibitors of MT polymerization could decrease MT polymerization rate in *Pten* KO growth cones to WT levels. We performed a dose–response with 1–10 nM vinblastine and imaged culture dishes immediately following drug administration for up to 4 h. We found acute inhibition of MT polymerization with 1–10 nM vinblastine was sufficient to reduce MT polymerization rate in *Pten* KO cultures in a dose dependent fashion [KO Veh = 0.118 ± 0.007 μm/s (19) vs KO 1 nM Vin = 0.099 ± 0.004 μm/s (18); $p = 0.051$, KO Veh vs KO 2 nM Vin = 0.075 ± 0.003 μm/s (11); $p = 0.0001$, KO Veh vs KO 5 nM Vin = 0.062 ± 0.002 μm/s (14); $p = 0.0001$, KO Veh vs KO 10 nM Vin = 0.058 ± 0.003 μm/s (2); $p = 0.0007$, two-way ANOVA with Bonferroni's *post hoc*; Fig. 8*A*,*B*]. We found 1 and 2 nM vinblastine was sufficient to reduce MT polymerization rate to WT levels [WT Veh = 0.091 ± 0.003 μm/s (22) vs KO 1 nM Vin = 0.099 ± 0.004 μm/s (18); $p = 0.999$, WT Veh vs KO 2 nM Vin = 0.075 ± 0.003 μm/s (11); $p = 0.583$, two-way ANOVA with Bonferroni's *post hoc*; Fig. 8*B*]; additionally, 1 nM vinblastine did not impact MT polymerization rate in WT cultures [WT Veh = 0.091 ± 0.003 μm/s (22) vs WT 1 nM Vin = 0.090 ± 0.005 μm/s (16); $p = 0.999$, two-way ANOVA with Bonferroni's *post hoc*]. Therefore, these data suggest that acute inhibition of MT polymerization, with low doses of vinblastine, is sufficient to reduce MT polymerization rate to WT levels in neurons with *Pten* deletion.

We next hypothesized that reducing the MT polymerization rate to WT levels is sufficient to reduce dendritic overgrowth in *Pten* KO neurons. To do this, we administered 1 nM vinblastine to WT and *Pten* KO cultures from 5 to 12 DIV and reconstructed the dendritic arbors of treated neurons (Fig. 8*C*). Sholl analysis revealed 1 nM vinblastine was sufficient to reduce number of intersections in *Pten* KO neurons, as compared with vehicle-treated KO (KO Veh vs KO 1 nM Vin $p = 0.001$, two-way ANOVA with Bonferroni's *post hoc*; Fig. 8*D*). Further, 1 nM vinblastine was sufficient to reduce Sholl of intersections to the level of WT-vehicle-treated neurons (KO 1 nM Vin vs WT Veh $p = 0.999$, two-way ANOVA with Bonferroni's *post hoc*; Fig. 8*D*), while having no significant impact on Sholl of intersections in WT-1 nM vinblastine-treated neurons (WT 1 nM Vin vs WT Veh $p = 0.999$, two-way ANOVA with Bonferroni's *post hoc*; Fig. 8*D*). Finally, we examined total dendritic length to find that 1 nM vinblastine was sufficient to reduce total dendritic length of *Pten* KO neurons to vehicle-treated WT levels [KO Veh = 1727 ± 215 μm (24) vs KO 1 nM Vin = 905.8 ± 91.4 μm (20); $p = 0.002$; WT Veh = 1265 ± 126 μm (17) vs KO 1 nM Vin; $p = 0.80$]. Vinblastine did not impact total dendritic length of treated WT neurons [WT Veh vs WT 1 nm Vin = 1126 ± 134 μm (20); $p = 0.999$, two-way ANOVA with Bonferroni's *post hoc*; Fig. 8*E*]. Taken together, these data indicate that reducing MT polymerization rate to WT levels is sufficient to rescue dendritic overgrowth in *Pten* KO neurons.

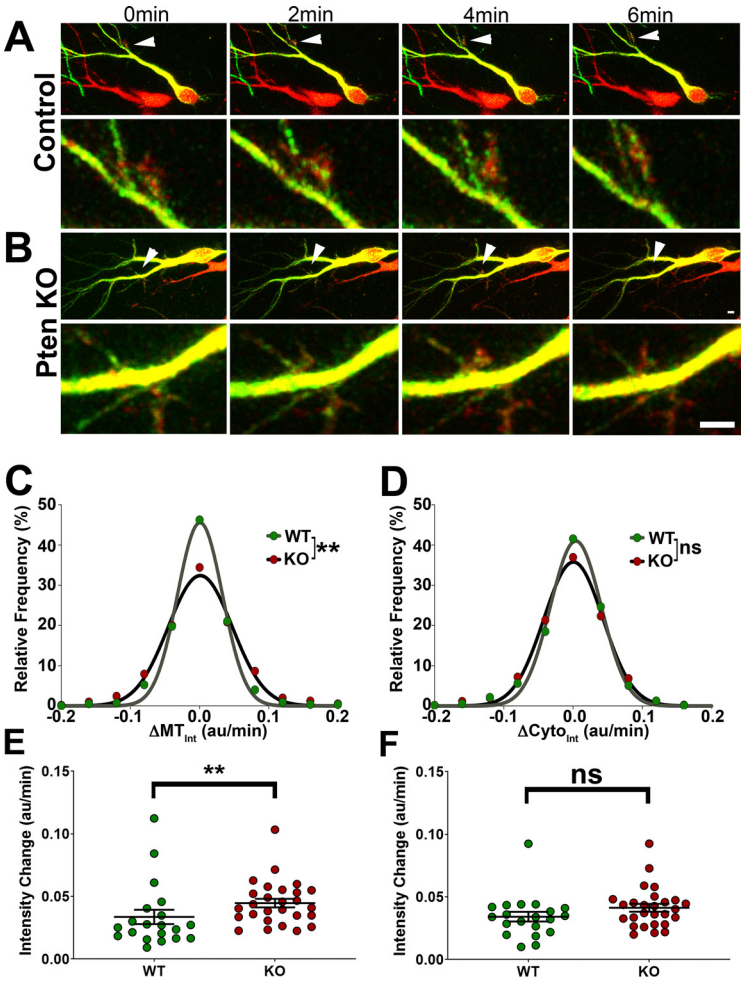

Figure 6. *Pten* KO growth cones have more dynamic MTs. Retroviruses labeling the MT plus-end binding protein (EB3-GFP) were co-injected with mCherry-T2A-Cre-expressing retroviruses into the hippocampal dentate gyrus of either tdTomato(Ai14) $^{Flox/Flo}$ x or *Pten* $^{Flox/Flox}$ x tdTomato(Ai14) $^{Flox/Flox}$ mice at P7. Two color two-photon imaging allowed us to track MT dynamics in sprouting growth cones (arrowheads in top panels and zoomed in view in bottom panels) for control (***A***) and *Pten* KO (***B***) neurons. We analyzed the change in MT [$\Delta MT_{Int} = (t_2MT_{Int} - t_1MT_{Int})/t_1Cyto_{Int}$] or cytoplasmic [$\Delta Cyto_{Int} = (t_2Cyto_{Int} - t_1Cyto_{Int})/t_1Cyto_{Int}$] signal intensity over the lifetime of individual processes. MT (***C***; ΔMT_{Int}) and cytoplasmic (***D***; $\Delta Cyto_{Int}$) intensity changes were plotted in a histogram and the distribution was fit with a Gaussian function (ΔMT_{Int} R^2 WT: 0.99, KO: 0.98; $\Delta Cyto_{Int}$ R^2 WT: 0.99, KO: 0.99). There was a broader distribution of MT intensity change within *Pten* KO processes, as compared with control ($^{**}p = 0.005$, Kolmogorov–Smirnov test; WT: 551 processes, KO: 1109 processes; ***C***). However, there was no difference in cytoplasmic intensity change within nascent dendritic processes of *Pten* KO and control neurons ($^{ns}p = 0.184$, Kolmogorov–Smirnov test; WT: 551 processes, KO: 1109 processes; ***D***). We also examined the MT (***E***; ΔMT_{Int}) and cytoplasmic (***F***; $\Delta Cyto_{Int}$) intensity changes as an average of the absolute value of intensity change per cell. Each dot on the histogram indicates a single cell, we again found an increase in intensity change for the MT (***E***) but not cytoplasmic (***F***) markers ($^{**}p < 0.01$ Mann–Whitney test). Scale bars: 5 μm.

Vinblastine rescues dendritic overgrowth of *pten* KO neurons *in vivo*

We next examined the effect of vinblastine treatment *in vivo*, the *Pten*$^{flox/flox}$ animals were co-injected into the dentate gyrus with a retrovirus expressing Cre with mCherry, and a GFP-control retrovirus with no Cre at P7. Vinblastine (0.1 mg/kg body weight) was administered intrathecally every 72 h from 3 to 21 DPI. Animals were perfused on 21 DPI and neurons were analyzed (Fig. 9*A*,*B*). We measured soma cross sectional area and

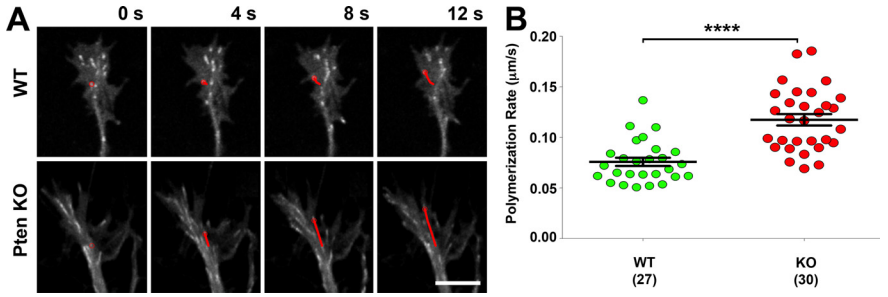

Figure 7. *Pten* KO dendritic growth cones have increased rate of MT polymerization. Primary cultured hippocampal neurons were generated from either *Pten* $^{Flox/Flox}$ or *Pten* $^{Flox/Flox}$x tdTomato(Ai14)$^{Flox/Flox}$ mice at P0/1. Cultures were co-transfected with either mCherry-T2A-Cre (*Pten* KO)- or RedRubi (mCherry-expressing; WT)- plasmid and a plasmid to tag the plus-end MTs (EB3-GFP) at 4 DIV. Dendritic growth cones were imaged for 10 min at a rate of 15 Hz between 5 and 7 DIV. EB3 puncta were tracked over time to measure MT polymerization rate (red line; ***A***). *Pten* KO dendritic growth cones showed an increased MT polymerization rate, as compared with WT (***B***). Numbers along the top right corner of the panels in ***A*** represent time. Scale bar: 5 μm. Numbers in parenthesis indicate cell number (*$p < 0.05$, **$p < 0.01$, ***$p < 0.001$, ****$p < 0.0001$; unpaired *t* test with Welch's correction).

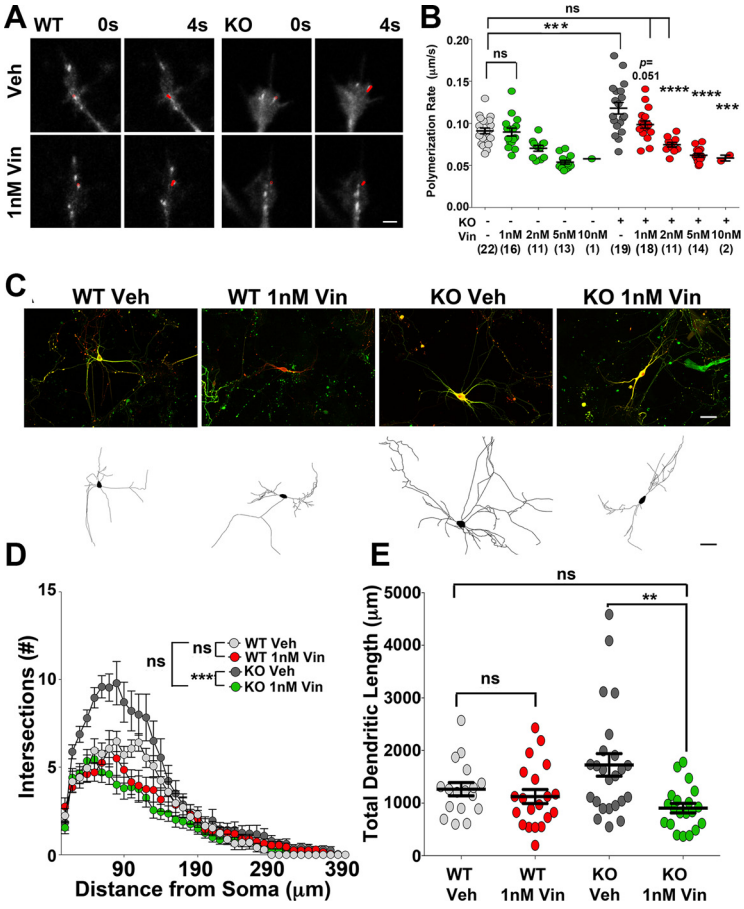

Figure 8. Reducing MT polymerization rate rescues dendritic over-growth of *Pten* KO neurons. WT and KO hippocampal cultures were treated with 1–10 nM vinblastine for up to 4 h and MT polymerization rate was measured (red lines; ***A***). There was an increased MT polymerization rate within dendritic growth cones from vehicle-treated *Pten* KO cultures, as compared with vehicle-treated WT cultures (*Pten* KO: VEH vs WT: VEH; ***B***). Acute treatment with vinblastine at 1–10 nM was sufficient to reduce MT polymerization rate in a dose-dependent fashion in *Pten* KO neurons (***B***); 1 and 2 nM vinblastine was sufficient to reduce MT polymerization rate in *Pten* KO dendritic growth cones to the level of vehicle-treated WT (***B***). *Pten* KO and WT cultures were treated from 5 to 12 DIV with 1 nM vinblastine and reconstructed using Neurolucida (***C***). Chronic inhibition of MT polymerization, via 1 nM vinblastine, was sufficient to reduce Sholl of intersections in *Pten* KO neurons, as compared with vehicle-treated KO neurons (***D***). Further, chronic treatment with 1 nM vinblastine was sufficient to reduce Sholl of intersection in KO neurons to vehicle-treated WT levels, without significantly impacting the number of intersections in WT 1 nM vinblastine-treated neurons (***D***). Chronic 1 nM vinblastine was also sufficient to reduce total dendritic length in *Pten* KO neurons to WT vehicle-treated neuron levels without impacting total dendritic length in WT neurons (***E***) Numbers along the top right corner of the panels in ***A*** represent time. Scale bar: 2.5 μm (***A***) and 50 μm (***C***). Numbers in parenthesis indicate cell number (*$p < 0.05$, **$p < 0.01$, ***$p < 0.001$, ****$p < 0.0001$; two-way ANOVA with Bonferroni's *post hoc*).

found that vinblastine had no effect on soma hypertrophy [WT vehicle = 107.5 ± 2.065 μm (83) vs WT vinblastine = 105.8 ± 1.810 μm (138), $p > 0.05$; KO vehicle = 253.7 ± 8.133 μm (69) vs KO vinblastine = 243.5 ± 5.339 μm (143), $p > 0.05$; mixed effect model]. We next examined the position of the neurons in the GCL and also found no effect on migration of the granule neurons [WT vehicle = 31.78 ± 1.114% (84) vs WT vinblastine = 29.80 ± 0.837% (135) $p > 0.05$; KO vehicle = 53.84 ± 1.17% (67) vs KO vinblastine = 53.22 ± 1.09% (135), $p > 0.05$]. Vinblastine treatment was sufficient to reduce total dendritic length of *Pten* KO neurons as compared with *Pten* KO neurons from vehicle-treated animals [Veh KO = 1620 ± 320 μm (26) vs Vin KO = 1325 ± 415.1 μm (36); $p = 0.0051$; Figs. 9*C*, 10]. Further, this dose of vinblastine had no impact on the total dendritic length of WT neurons [Veh Cont = 1145.3 ± 36.4 μm (23) vs Vin Cont = 1045.4 ± 269.7 μm (28); $p = 0.717$]. *Pten* KO neurons from vinblastine-treated animals had a reduced Sholl of intersections as compared with *Pten* KO neurons from vehicle-treated animals (Vin KO vs Veh KO, $p = 0.002$; Fig. 9*D*), while vinblastine-treatment did not affect the Sholl of intersections of WT neurons (Veh Cont vs Vin Cont, $p > 0.9$; Fig. 9*D*). This vinblastine-mediated reduction of overgrowth in *Pten* KO neurons was found starting from a distance of 90 μm from soma, when compared with vehicle-treated control neurons (Veh Cont vs Vin KO, $p = 0.321$; Fig. 9*D*). Vinblastine-treatment did not impact the sprouting of primary dendrites of *Pten* KO neurons but did reduce the increased distal branching as indicated by the Sholl of intersections (Fig. 9*D*) and confirmed by quantification of nodes and ends (data not shown). These data indicate that vinblastine treatment reduces the dendritic overgrowth of *Pten* KO neurons to that of WT neurons *in vivo*.

Vinblastine improves spatial memory in *pten* KO mice

The interaction of Treatment (untreated and Vinblastine-treated) with Group (Control, *Pten* KO) was statistically analyzed via General Estimating Equations (GEE) for the number of goal zone entrances in each visible and hidden goal session (Fig. 11*A*,*B*). Individual examples of performance in each condition are shown in Figure 11 for untreated controls (Fig. 11*C*), vinblastine-treated *Pten*

KO mice (Fig. 11*D*), and untreated *Pten* KO mice (Fig. 11*E*).

Visible goal sessions

No significant Treatment × Group interactions were found for the number of goal zone entrances during the visible goal version of the spatial accuracy task in the standard goal location (V1; Wald Value = 7.1, $p = 0.069$), the second (V3; Wald Value = 0.79, $p = 0.852$) and third (V4; Wald Value = 2.08, $p = 0.555$) goal rotation sessions (Fig. 11*G*). A significant Treatment × Group interaction was found in the first visible goal rotation session (V2; Wald Value = 8.26, $p = 0.041$; [Untreated × Cont] Wald Value = 0a; [Untreated × Pten] Wald Value = 0.073, $p = 0.787$; [Vin × Cont] Wald Value = 6.58, $p = 0.01$; [Vin × Pten ko] Wald Value = 0.062, $p = 0.803$) where vinblastine-treated controls made significantly fewer goal zone entrances than untreated controls (Fig. 11*A*). *Pten* KO and vinblastine treatment therefore generally did not impede the association of the visible goal object with reward when placed in multiple spatial locations. While treated controls may have been sensitive to the first goal rotation, they were similar to untreated controls thereafter.

Hidden goal sessions

A significant Treatment × Group interaction was found for the number of goal zone entrances during the hidden goal version of the spatial accuracy task in the standard goal location (H1; Wald Value = 10.12, $p = 0.018$; [Untreated × Cont] Wald Value = 0a; [Untreated × *Pten* KO] Wald Value = 0.504, $p = 0.005$; [Vin × Cont] Wald Value = 8.57, $p = 0.003$; [Vin × *Pten* KO] Wald Value = 0.876, $p = 0.349$). Both acutely vinblastine-treated *Pten* KO and chronically vinblastine-treated controls made significantly fewer entrances than untreated controls (Fig. 11*B*).

There were significant Treatment × Group interactions during the first hidden goal rotation (H2; Wald Value = 11.06, $p = 0.011$; [Untreated × Cont] Wald Value = 0a; [Untreated × Pten] Wald Value = 7.76, $p = 0.005$; [Vin × Cont] Wald Value = 4.97, $p = 0.026$; [Vin × *Pten* KO] Wald Value = 0.047, $p = 0.828$) and during the second hidden goal rotation (H3; Wald Value = 8.31, $p = 0.04$; [Untreated × Cont] Wald Value = 0a; [Untreated × Pten KO] Wald Value = 5.00, $p = 0.025$; [Vin × Cont] Wald Value = 0.02, $p = 0.969$; [Vin × *Pten* KO] Wald Value = 0.006, $p = 0.937$). In the first rotation

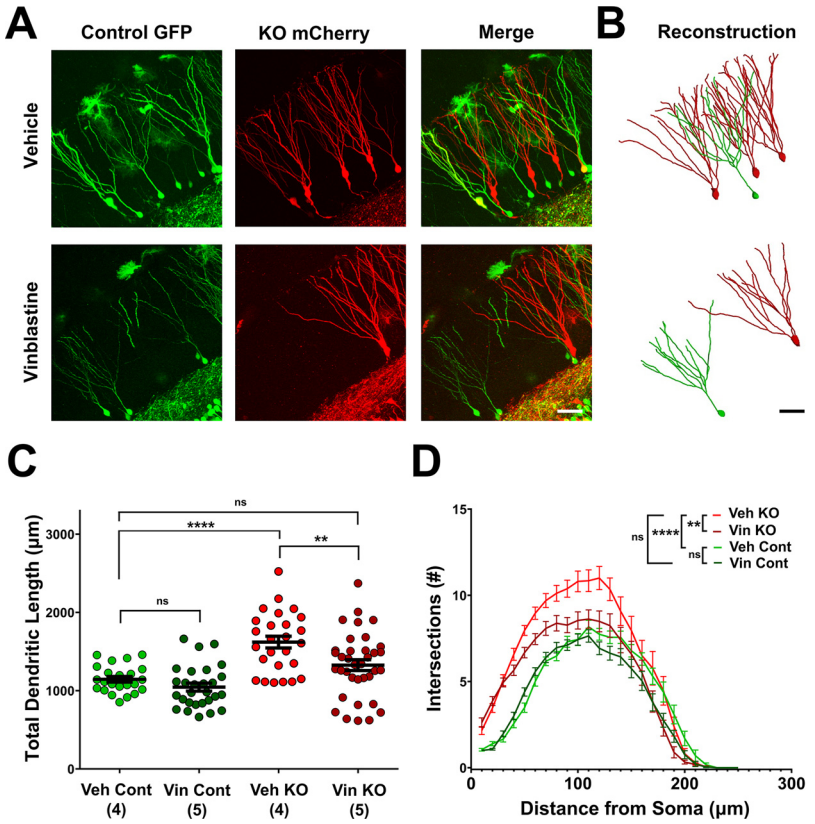

Figure 9. Reducing MT polymerization rate rescues dendritic overgrowth of *Pten* KO neurons *in vivo*. The hippocampal dentate gyrus of P7 $Pten^{Flox/Flox}$ mice was injected with a retrovirus expressing mCherry and Cre to label *Pten* KO neurons and a retrovirus that expressed GFP to label control cells (***A***). Vinblastine (0.1 mg/kg by weight) was administered intrathecally every 72 h from 10 to 18 DPI, and the animals were perfused and neuronal reconstructions generated at 21 DPI (***B***). All Neurolucida reconstructions can be seen in Figure 10. Increased total dendritic length of *Pten* KO neurons was rescued by vinblastine treatment with no significant impact on vehicle-treated WT neurons (***C***). Further, vinblastine-mediated inhibition of MT polymerization reduced overall Sholl of intersections in *Pten* KO neurons, in comparison to vehicle-treated KO neurons (***D***). Scale bar: 50 µm; $*p < 0.05$, $**p < 0.01$, $***p < 0.001$, $****p < 0.0001$ using a mixed-effect model and pwcompare.

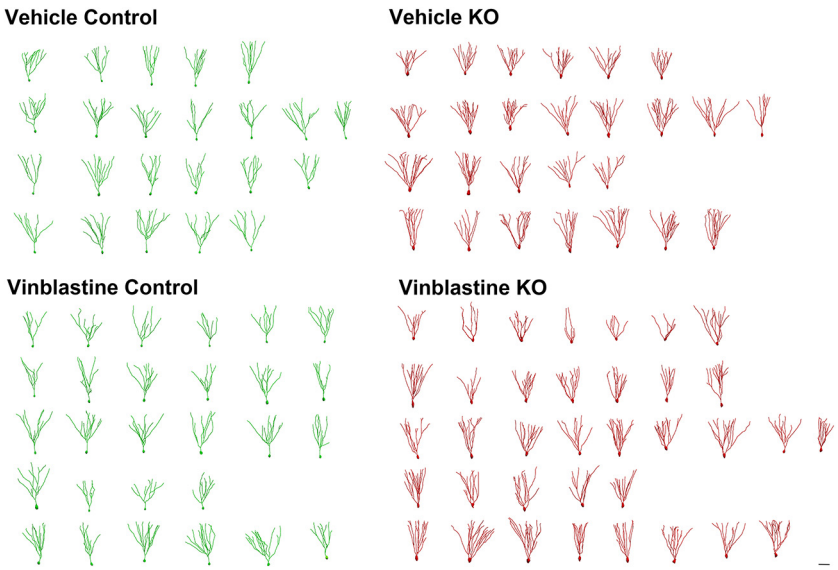

Figure 10. All Neurolucida 360 reconstructions of dendritic arbors *in vivo*. Neuronal reconstructions from mice treated with vehicle or vinblastine for fluorophore-only expressing neurons (control) and $Pten^{flx/flx}$; Cre+ (KO) neurons. Each row contains reconstructions from one individual animal. Scale bar: 50 µm.

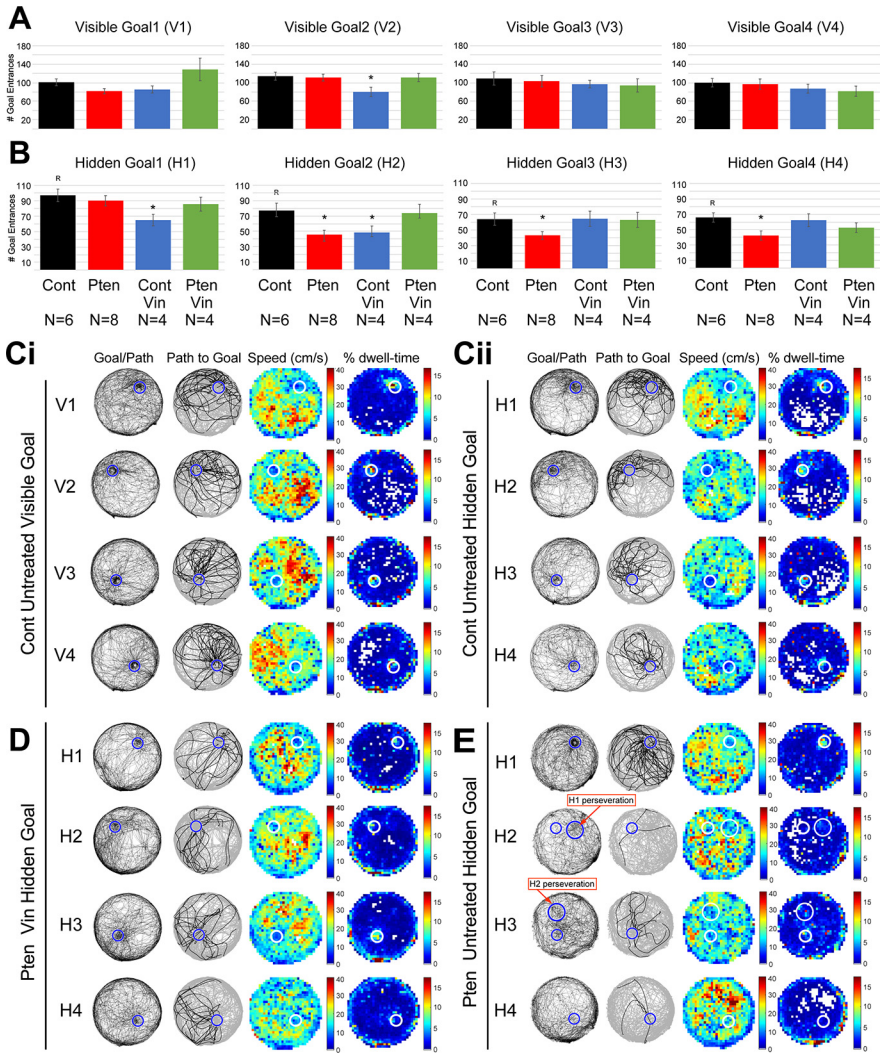

Figure 11. The effect of *Pten* KO and vinblastine treatment on spatial memory. Referenced to untreated controls, all groups showed a similar number of mean entrances in the standard visible goal location (V1) and the second (V3) and third (V4) rotation sessions. Yet, in the first rotation session (V2) both vinblastine-treated controls made significantly fewer goal zone entrances than untreated controls (***A***). Relative to untreated controls, vinblastine-treated *Pten* KO mice had similar levels of goal zone entrances across hidden goal sessions while untreated *Pten* KO mice made significantly fewer entrances across rotation sessions (***B***). Untreated *Pten* KO mice exhibited an enduring deficit in associating the visible object cue with novel spatial locations (***B***, H2–H4). Vinblastine treatment may have negatively impacted control mice as hidden goal performance was significantly lower than untreated controls in baseline and the first rotation session (***B***, H1–H2). However, performance in these mice improved by the second and third rotation sessions (***B***, H3–H4). R = reference comparator for GEE statistics. Examples of goal and path, path to goal, speed (cm/s) and percent dwell-time during performance for an individual mouse in the visible (V-Left) and hidden (H-Right) spatial accuracy conditions (***C–E***). Neither untreated control (***C***) or vinblastine-treated *Pten* KO mice (***D***) exhibited spatial accuracy deficits in either spatial accuracy condition while untreated *Pten* KO mice (***E***) made significantly fewer goal zone entrances because of a tendency for perseverating on previous goal zone locations (larger circles) rather than the zone in the visible cue session just minutes prior (smaller circles).

session, all groups but the vinblastine-treated mice made significantly fewer entrances than untreated controls (Fig. 11*B*). In the second rotation session, the vinblastine-treated control mice began to improve performance while untreated *Pten* KO and acutely vinblastine-treated mice performance remained poor Figure 11*B*. While the Treatment × Group interaction was marginal during the final rotation session (H4; Wald Value = 7.72, $p = 0.052$), performance in untreated *Pten* KO mice remained significantly worse than untreated controls (Fig. 11*B*; [Untreated × Cont] Wald Value = 0a; [Untreated × Pten KO] Wald Value = 6.79, $p = 0.009$; [Vin × Cont] Wald Value = 0.119, $p = 0.731$; [Vin × *Pten* KO] Wald Value = 2.275, $p = 0.131$).

The results indicate that *Pten* KO causes a unique spatial cognitive deficit that impedes the flexible association of a visible object cue with multiple, novel spatial locations. Vinblastine treatment both rescued dendritic overgrowth and prevented this cognitive deficit in *Pten* KO mice. Vinblastine treatment in controls may have had adverse effects on spatial processing as these animals performed worse than untreated controls in baseline training and the first rotation session. However, these mice were able to improve performance by the second rotation session.

Discussion

Pten loss leads to dendritic overgrowth. Here, we demonstrate that *Pten* KO neurons sprout more new processes and have increased MT polymerization rate within those processes. Further, we showed that reducing MT polymerization rate is sufficient to reduce dendritic overgrowth in *Pten* KO neurons. Interestingly, *in vivo* we found that vinblastine treatment did not reduce the soma size, migration distance, or number of primary dendrites arising directly from the soma but was able to reduce the number of branches and overall length of the dendritic arbor. This effect could be because vinblastine treatment was started shortly after phenotype onset (3 d after retrovirus injection) or indicate a distinct mechanism for soma hypertrophy, migration and sprouting of dendrites versus branch formation along nascent dendrites.

Dendritogenesis occurs through the regulation of protein translation and cytoskeletal remodeling in response to cell intrinsic and extrinsic cues. *Pten* KO neurons form more new processes per micrometer per hour, as compared with WT. New process formation, collapse, or stabilization is regulated by cell extrinsic cues including GABA, glutamate, and neurotrophins that are responsive to developmental brain activity (Cline and Haas, 2008; Cheng and Poo, 2012; Puram and Bonni, 2013). BDNF has been shown to elicit spatially restricted dendritic growth at crossings of BDNF-overexpressing axons (Horch and Katz, 2002). Receptor tyrosine kinases elicit PIP3 accumulation, transient actin patch formation, followed by f-actin bundling and polymerization and formation of an f-actin enriched filopodia (Luikart et al., 2008; Gallo, 2013; Sainath and Gallo, 2015). The loss of PTEN-dependent PIP3 catalysis allows the sprouting of filopodial and dendritic growth cones to occur in an unregulated fashion. We demonstrate that PTEN-loss allows for increased MT polymerization into motile dendritic

growth cones promoting increased dendritic arborization and branching of developing neurons.

We show that *Pten* loss leads to increased MT polymerization rate and reducing MT polymerization rate to WT levels is sufficient to reduce dendritic overgrowth *in vitro* and *in vivo*. In neurons, PTEN has been shown to co-localize with MTs (Chadborn et al., 2006; Kreis et al., 2014), and *Pten* loss leads to changes to MT posttranslational modifications (Cupolillo et al., 2016; Kath et al., 2018). Interestingly, enhanced axonal outgrowth in *Pten* null neurons can be ameliorated via increasing levels of detyrosinated tubulin (Kath et al., 2018). However, the detailed mechanism through which *Pten* loss regulates MT polymerization rate is unclear. Based on our *in vitro* experiments, PTEN is unlikely to affect MT dynamics through its actions on mTOR signaling, as acute inhibition of mTORC1, and protein synthesis do not reduce MT polymerization rate. The effect on dendritic arborization may extend to dendritic spine formation and stabilization as postsynaptic PTEN regulation of the cytoskeleton impacts excitatory synapse formation (Jiang et al., 2021). It will be important to determine whether chronic inhibition of mTOR can impact cytoskeletal polymerization rate.

The therapeutic potential of targeting MT polymerization is strongly suggested by the improved spatial cognitive outcomes in the vinblastine-treated *Pten* KO animals. An inability to flexibly associate an object with novel spatial locations in *Pten* KO mice may be because of altered functionality in the medial molecular layer (MML) and outer molecular layer (OML) dentate gyrus synapses. A recent study showed that object learning necessitated slow γ coupling between the lateral entorhinal cortex and OML while pure spatial learning required medium γ coupling with the MML (Fernández-Ruiz et al., 2021). Future studies will examine structure and function relationships between dendritic overgrowth at key entorhinal-dentate gyrus synapses and. Importantly, our results indicate that morphologic changes localized to the dentate gyrus are sufficient for causing spatial memory deficits and that reversing them can rescue spatial deficits. This result has broad implications for understanding the relationship between pathologic electrographic activity, the impairment of neurophysiology underlying key neocortical-hippocampal synapses and flexible spatial outcomes. The tendency for *Pten* KO mice to perseverate on older training locations is also reminiscent of the fMR1 mouse model of autism, where mice are unable to escape a shock zone on an arena once it has been moved to a new location (Radwan et al., 2016). It should be noted that there was decreased performance of WT mice treated with vinblastine. It is well known that vinblastine results in cognitive deficits in individuals undergoing chemotherapy. Our use of vinblastine in this study provides a proof of principal for molecular targeting of MTs, not an indication of vinblastine itself as a treatment.

Our *in vivo* and *in vitro* data demonstrate that low doses of vinblastine are sufficient to decrease dendritic elaboration induced by *Pten* dysfunction. These doses do not interfere with MT dynamics in WT neurons, which suggests that there is a therapeutic window for rescue of dendritic arborization that can be achieved using MT targeting drugs. It has previously been shown that reducing increased protein translation *in vitro* and *in vivo* is sufficient to reduce dendritic overgrowth (Jaworski et al., 2005; Zhou et al., 2009; Weston et al., 2012; Haws et al., 2014; Lin et al., 2016). This suggests that there are at least two independent pathways that could be targeted for therapeutic gain. This opens the possibility for an intersectional approach targeting MT polymerization and mTOR with low doses of inhibitors to achieve treatment with minimal side effects.

References

Bures J, Fenton AA, Kaminsky Y, Rossier J, Sacchetti B, Zinyuk L (1997) Dissociation of exteroceptive and idiothetic orientation cues: effect on hippocampal place cells and place navigation. Philos Trans R Soc Lond B Biol Sci 352:1515–1524.

Butler MG, Dasouki MJ, Zhou XP, Talebizadeh Z, Brown M, Takahashi TN, Miles JH, Wang CH, Stratton R, Pilarski R, Eng C (2005) Subset of individuals with autism spectrum disorders and extreme macrocephaly associated with germline PTEN tumour suppressor gene mutations. J Med Genet 42:318–321.

Buxbaum JD, Cai G, Chaste P, Nygren G, Goldsmith J, Reichert J, Anckarsäter H, Rastam M, Smith CJ, Silverman JM, Hollander E, Leboyer M, Gillberg C, Verloes A, Betancur C (2007) Mutation screening of the PTEN gene in patients with autism spectrum disorders and macrocephaly. Am J Med Genet B Neuropsychiatr Genet 144B:484–491.

Chalhoub N, Baker SJ (2009) PTEN and the PI3-kinase pathway in cancer. Annu Rev Pathol 4:127–150.

Chadborn NH, Ahmed AI, Holt MR, Prinjha R, Dunn GA, Jones GE, Eickholt BJ (2006) PTEN couples Sema3A signalling to growth cone collapse. J Cell Sci 119:951–957.

Cheng PL, Poo MM (2012) Early events in axon/dendrite polarization. Annu Rev Neurosci 35:181–201.

Cline H, Haas K (2008) The regulation of dendritic arbor development and plasticity by glutamatergic synaptic input: a review of the synaptotrophic hypothesis. J Physiol 586:1509–1517.

Clipperton-Allen AE, Page DT (2014) Pten haploinsufficient mice show broad brain overgrowth but selective impairments in autism-relevant behavioral tests. Hum Mol Genet 23:3490–3505.

Cupolillo D, Hoxha E, Faralli A, De Luca A, Rossi F, Tempia F, Carulli D (2016) Autistic-like traits and cerebellar dysfunction in Purkinje cell PTEN knock-out mice. Neuropsychopharmacology 41:1457–1466.

Endersby R, Baker SJ (2008) PTEN signaling in brain: neuropathology and tumorigenesis. Oncogene 27:5416–5430.

Eng C (2003) PTEN: one gene, many syndromes. Hum Mutat 22:183–198.

Fernández-Ruiz A, Oliva A, Soula M, Rocha-Almeida F, Nagy GA, Martin-Vazquez G, Buzsáki G (2021) Gamma rhythm communication between entorhinal cortex and dentate gyrus neuronal assemblies. Science 372: eabf3119.

Fricano CJ, Despenza T Jr, Frazel PW, Li M, O'Malley AJ, Westbrook GL, Luikart BW (2014) Fatty acids increase neuronal hypertrophy of Pten knockdown neurons. Front Mol Neurosci 7:30.

Fricano-Kugler CJ, Williams MR, Salinaro JR, Li M, Luikart B (2016) Designing, packaging, and delivery of high titer CRISPR retro and lentiviruses via stereotaxic injection. J Vis Exp (111):53783.

Fricano-Kugler CJ, Getz SA, Williams MR, Zurawel AA, DeSpenza T Jr, Frazel PW, Li M, O'Malley AJ, Moen EL, Luikart BW (2018) Nuclear excluded autism-associated phosphatase and tensin homolog mutations dysregulate neuronal growth. Biol Psychiatry 84:265–277.

Gallo G (2013) Mechanisms underlying the initiation and dynamics of neuronal filopodia: from neurite formation to synaptogenesis. Int Rev Cell Mol Biol 301:95–156.

Getz SA, DeSpenza T Jr, Li M, Luikart BW (2016) Rapamycin prevents, but does not reverse, aberrant migration in Pten knockout neurons. Neurobiol Dis 93:12–20.

Hansen-Kiss E, Beinkampen S, Adler B, Frazier T, Prior T, Erdman S, Eng C, Herman G (2017) A retrospective chart review of the features of PTEN hamartoma tumour syndrome in children. J Med Genet 54:471–478.

Haws ME, Jaramillo TC, Espinosa F, Widman AJ, Stuber GD, Sparta DR, Tye KM, Russo SJ, Parada LF, Stavarache M, Kaplitt M, Bonci A, Powell CM (2014) PTEN knockdown alters dendritic spine/protrusion morphology, not density. J Comp Neurol 522:1171–1190.

Horch HW, Katz LC (2002) BDNF release from single cells elicits local dendritic growth in nearby neurons. Nat Neurosci 5:1177–1184.

Jaworski J, Spangler S, Seeburg DP, Hoogenraad CC, Sheng M (2005) Control of dendritic arborization by the phosphoinositide-3'-kinase-Akt-mammalian target of rapamycin pathway. J Neurosci 25:11300–11312.

Jiang X, Sando R, Sudhof TC (2021) Multiple signaling pathways are essential for synapse formation induced by synaptic adhesion molecules. Proc Natl Acad Sci USA 118:e2000173118.

Kath C, Goni-Oliver P, Müller R, Schultz C, Haucke V, Eickholt B, Schmoranzer J (2018) PTEN suppresses axon outgrowth by down-regulating the level of detyrosinated microtubules. PLoS One 13:e0193257.

Ketschek A, Gallo G (2010) Nerve growth factor induces axonal filopodia through localized microdomains of phosphoinositide 3-kinase activity that drive the formation of cytoskeletal precursors to filopodia. J Neurosci 30:12185–12197.

Kreis P, Leondaritis G, Lieberam I, Eickholt BJ (2014) Subcellular targeting and dynamic regulation of PTEN: implications for neuronal cells and neurological disorders. Front Mol Neurosci 7:23.

Kubie JL, Fenton A, Novikov N, Touretzky D, Muller RU (2007) Changes in goal selection induced by cue conflicts are in register with predictions from changes in place cell field locations. Behav Neurosci 121:751–763.

Kumar V, Zhang MX, Swank MW, Kunz J, Wu GY (2005) Regulation of dendritic morphogenesis by Ras-PI3K-Akt-mTOR and Ras-MAPK signaling pathways. J Neurosci 25:11288–11299.

Kwon CH, Luikart BW, Powell CM, Zhou J, Matheny SA, Zhang W, Li Y, Baker SJ, Parada LF (2006) Pten regulates neuronal arborization and social interaction in mice. Neuron 50:377–388.

Lenck-Santini PP, Save E, Poucet B (2001) Evidence for a relationship between place-cell spatial firing and spatial memory performance. Hippocampus 11:377–390.

Lin TV, Hsieh L, Kimura T, Malone TJ, Bordey A (2016) Normalizing translation through 4E-BP prevents mTOR-driven cortical mislamination and ameliorates aberrant neuron integration. Proc Natl Acad Sci USA 113:11330–11335.

Luikart BW, Zhang W, Wayman GA, Kwon CH, Westbrook GL, Parada LF (2008) Neurotrophin-dependent dendritic filopodial motility: a convergence on PI3K signaling. J Neurosci 28:7006–7012.

Luikart BW, Schnell E, Washburn EK, Bensen AL, Tovar KR, Westbrook GL (2011a) Pten knockdown in vivo increases excitatory drive onto dentate granule cells. J Neurosci 31:4345–4354.

Luikart BW, Bensen AL, Washburn EK, Perederiy JV, Su KG, Li Y, Kernie SG, Parada LF, Westbrook GL (2011b) miR-132 mediates the integration of newborn neurons into the adult dentate gyrus. PLoS One 6:e19077.

Meijering E, Dzyubachyk O, Smal I (2012) Methods for cell and particle tracking. Methods Enzymol 504:183–200.

Miller AL, Bement WM (2009) Regulation of cytokinesis by Rho GTPase flux. Nat Cell Biol 11:71–77.

Moen EL, Fricano-Kugler CJ, Luikart BW, O'Malley AJ (2016) Analyzing Clustered Data: Why and How to Account for Multiple Observations Nested within a Study Participant? PloS one 11:e0146721.

Morris RG, Garrud P, Rawlins JN, O'Keefe J (1982) Place navigation impaired in rats with hippocampal lesions. Nature 297:681–683.

Mouchati PR, Kloc ML, Holmes GL, White SL, Barry JM (2020) Optogenetic "low-theta" pacing of the septohippocampal circuit is sufficient for spatial goal finding and is influenced by behavioral state and cognitive demand. Hippocampus 30:1167–1193.

Perederiy JV, Luikart BW, Washburn EK, Schnell E, Westbrook GL (2013) Neural injury alters proliferation and integration of adult-generated neurons in the dentate gyrus. J Neurosci 33:4754–4767.

Puram SV, Bonni A (2013) Cell-intrinsic drivers of dendrite morphogenesis. Development 140:4657–4671.

Radwan B, Dvorak D, Fenton A (2016) Impaired cognitive discrimination and discoordination of coupled theta-gamma oscillations in Fmr1 knockout mice. Neurobiol Dis 88:125–138.

Roossien DH, Sadis BV, Yan Y, Webb JM, Min LY, Dizaji AS, Bogart LJ, Mazuski C, Huth RS, Stecher JS, Akula S, Shen F, Li Y, Xiao T, Vandenbrink M, Lichtman JW, Hensch TK, Herzog ED, Cai D (2019) Multispectral tracing in densely labeled mouse brain with nTracer. Bioinformatics 35:3544–3546.

Sainath R, Gallo G (2015) Cytoskeletal and signaling mechanisms of neurite formation. Cell Tissue Res 359:267–278.

Skelton PD, Frazel PW, Lee D, Suh H, Luikart BW (2019) Pten loss results in inappropriate excitatory connectivity. Mol Psychiatry 24:1627–1640.

Skelton PD, Poquerusse J, Salinaro JR, Li M, Luikart BW (2020) Activity-dependent dendritic elaboration requires Pten. Neurobiol Dis 134:104703.

Stepanova T, Slemmer J, Hoogenraad CC, Lansbergen G, Dortland B, De Zeeuw CI, Grosveld F, van Cappellen G, Akhmanova A, Galjart N (2003) Visualization of microtubule growth in cultured neurons via the use of EB3-GFP (end-binding protein 3-green fluorescent protein). J Neurosci 23:2655–2664.

Thévenaz P, Ruttimann UE, Unser M (1998) A pyramid approach to subpixel registration based on intensity. IEEE Trans Image Process 7:27–41.

Tilot AK, Gaugler MK, Yu Q, Romigh T, Yu W, Miller RH, Frazier TW 2nd, Eng C (2014) Germline disruption of Pten localization causes enhanced sex-dependent social motivation and increased glial production. Hum Mol Genet 23:3212–3227.

Weston MC, Chen H, Swann JW (2012) Multiple roles for mammalian target of rapamycin signaling in both glutamatergic and GABAergic synaptic transmission. J Neurosci 32:11441–11452.

Williams MR, DeSpenza T Jr, Li M, Gulledge AT, Luikart BW (2015) Hyperactivity of newborn Pten knock-out neurons results from increased excitatory synaptic drive. J Neurosci 35:943–959.

Williams MR, Fricano-Kugler CJ, Getz SA, Skelton PD, Lee J, Rizzuto CP, Geller JS, Li M, Luikart BW (2016) A retroviral CRISPR-Cas9 system for cellular autism-associated phenotype discovery in developing neurons. Sci Rep 6:25611.

Zhou J, Blundell J, Ogawa S, Kwon CH, Zhang W, Sinton C, Powell CM, Parada LF (2009) Pharmacological inhibition of mTORC1 suppresses anatomical, cellular, and behavioral abnormalities in neural-specific Pten knock-out mice. J Neurosci 29:1773–1783.